PNAS RESEARCH ARTICLE | BIOPHYSICS AND COMPUTATIONAL BIOLOGY

Compression drives diverse transcriptomic and phenotypic adaptations in melanoma

Xingjian Zhang[a,b], Xin Shi[c], Dingyao Zhang[a], Xiangyu Gong[a], Zhang Wen[a], Israel Demandel[a], Junqi Zhang[a], Alejandro Rossello-Martinez[a], Trevor J. Chan[d], and Michael Mak[a,b,1]

Edited by Elliot Elson, Washington University in St Louis School of Medicine, St. Louis, MO; received November 25, 2022; accepted August 7, 2023

Physical forces are prominent during tumor progression. However, it is still unclear how they impact and drive the diverse phenotypes found in cancer. Here, we apply an integrative approach to investigate the impact of compression on melanoma cells. We apply bioinformatics to screen for the most significant compression-induced transcriptomic changes and investigate phenotypic responses. We show that compression-induced transcriptomic changes are associated with both improvement and worsening of patient prognoses. Phenotypically, volumetric compression inhibits cell proliferation and cell migration. It also induces organelle stress and intracellular oxidative stress and increases pigmentation in malignant melanoma cells and normal human melanocytes. Finally, cells that have undergone compression become more resistant to cisplatin treatment. Our findings indicate that volumetric compression is a double-edged sword for melanoma progression and drives tumor evolution.

biophysics | phenotype | melanoma | adaptation | compression

Significance

Physical forces are prominent in the tumor microenvironment and at various stages of tumor progression, but how physical forces impact and drive the emergence of diverse phenotypes in heterogeneous tumors is not well established. Here, we elucidate how melanoma cells adapt in response to compressive stress, which induces cell state changes including in transcriptional programs and drug response. Specifically, we demonstrate that volumetric compression, in particular via osmotic pressure, is a double-edged sword for melanoma progression and drives tumor evolution.

The survival and evolution of species are never easy. Darwin's theory of evolution emphasizes the significance of inherited variations and the adaptation to environmental changes as vital survival factors (1). In a tumor scenario, these two characteristics manifest as heterogeneity (2–4) and genetic and phenotypic plasticity (3, 5). As a tumor develops, melanoma cells may experience a range of environmental challenges that prompt adaptations. For instance, a previous study demonstrates that melanoma cells acquired a stem cell–like phenotype and enhanced tumorigenicity at the perimeter of tumor tissues (6). Melanoma cells have also been shown in another study to be able to undergo transitions to transient and persistent states of drug resistance (7).

Volumetric compression is a prominent biophysical cue that presents in cancer (8). The proliferation of tumor cells in constrained tissue environments leads to the compression of adjacent cells (9–12). Furthermore, during tumor progression and metastasis, cancer cells can migrate through dense matrices, intravasate and extravasate endothelial barriers, and finally colonize secondary sites (13). These events occur in confined microenvironments with cross-sectional areas that range from 10 to >300 μm^2 (14). To facilitate successful metastasis, cancer cells need to deform to migrate through subnucleus-scaled pores in the extracellular matrix (ECM) (15). The deformation of cancer cells (16) could lead to a decrease in cell volume (17, 18). In acral melanoma, cancer cells can also experience compression during routine activities such as walking (19). In addition to solid stresses, the tumor microenvironment is also subjected to elevated fluid pressure that can compress cells (20, 21).

Numerous studies have explored hyperosmolarity as a biocompatible stimulus for inducing controllable volumetric compression in various cell types such as mesenchymal stem cells (17, 22), adipocytes (23), breast cancer cells (8), lung cancer cells (24), and others (25). It has also been reported that volumetric compression induced by both osmotic and mechanical compression can enhance intestinal stem cell self-renewal and promote the formation of intestinal organoids via the activation of the Wnt/β-catenin pathway, indicating that they elicit similar mechanotransduction responses in cells (26). These findings provide further confirmation that cells are capable of exhibiting phenotypic and genetic plasticity in response to volumetric compression that can arise from multiple forms of stimuli (e.g., osmotic pressure, mechanical compression, etc.).

Priming cells with external physical stimuli (such as curvature, viscosity, and osmotic stress) has been indicated to be effective toward investigating their prolonged effects on different cell adaptations (6, 27, 28). However, the effects of volumetric compression on melanoma cells' adaptation and evolution have not been well established. Here, we evaluate the relationship of compression-induced melanoma phenotypic and transcriptomic evolutions to tumor progression and therapeutic outcomes. We primarily apply osmotic

Author affiliations: [a]Department of Biomedical Engineering, Yale University, New Haven, CT 06511; [b]Yale Cancer Center, Yale University, New Haven, CT 06511; [c]School of Chemical Engineering and Technology, Tianjin University, Tianjin 300350, China; and [d]Department of Bioengineering, University of Pennsylvania, Philadelphia, PA 19104

Author contributions: X.Z. and M.M. designed research; X.Z., X.S., D.Z., X.G., Z.W., I.D., J.Z., A.R.-M., T.J.C., and M.M. performed research; X.Z., D.Z., and M.M. analyzed data; and X.Z. and M.M. wrote the paper.

The authors declare no competing interest.

This article is a PNAS Direct Submission.

[1]To whom correspondence may be addressed. Email: michael.mak@yale.edu.

This article contains supporting information online at https://www.pnas.org/lookup/suppl/doi:10.1073/pnas.2220062120/-/DCSupplemental.

Published September 18, 2023.

pressure as the volumetric compression stimulus. We detect that transcriptomic changes in the compressed melanoma cells are associated with both improvements and worsening in patients' prognoses in the TCGA (The Cancer Genome Atlas) cutaneous melanoma (SKCM) dataset. We demonstrate that compressed cells have inhibited cell cycle, reduced migratory phenotype, increased organelle stress, and elevated oxidative stress. We show that compressed melanoma cells are more resistant to a subsequent treatment of cisplatin, leading to enhanced tumor cell survival. Overall, we find that compression induces both tumor-promoting and tumor-suppressing effects on melanoma progression.

Results

Volumetric Compression of Melanoma during Tumor Progression. There are many scenarios in which tumor cells can experience short- or long-term compression from their surroundings. At the primary site, tumor cells proliferate quickly inside a limited space and elevate cell–cell and cell–ECM compression. Using a spheroid model, we embed the YUMM (Yale University Mouse Melanoma 1.7) (29) cell spheroid in collagen gel. We show a positive correlation between the cell nucleus area and the cell's distance to the dense center of the spheroid (Fig. 1 *A*, *Upper*). To support the validity of the nucleus area as a predictor of cell volume, we further show the positive correlation between YUMM cell nucleus area and cell volume (Fig. 1 *A*, *Lower*). Aligned with a previous study (8), our results also indicate cancer cells are volumetrically compressed inside the tumor spheroid. In addition, volumetric compression may also occur when cells migrate through confined geometries, such as pores in the ECM (Fig. 1 *B*, *Upper*). Cell volume reduction was reported previously using a transwell assay that induces cell compression during invasion (18). Using our previously developed microfluidic device (30, 31), we show that the volume of a YUMMER (YUMM 1.7 Exposed to Radiation) (32) cell is reduced when compressed by confined geometry during migration (Fig. 1 *B*, *Lower*).

To modulate compression applied to cells in a controllable manner, here, we primarily utilize osmotic pressure. We add 2% polyethylene glycol 300 Da (PEG-300) or 4% PEG-300 in the medium to elevate the osmolality (*SI Appendix*, Fig. S1*A*). This

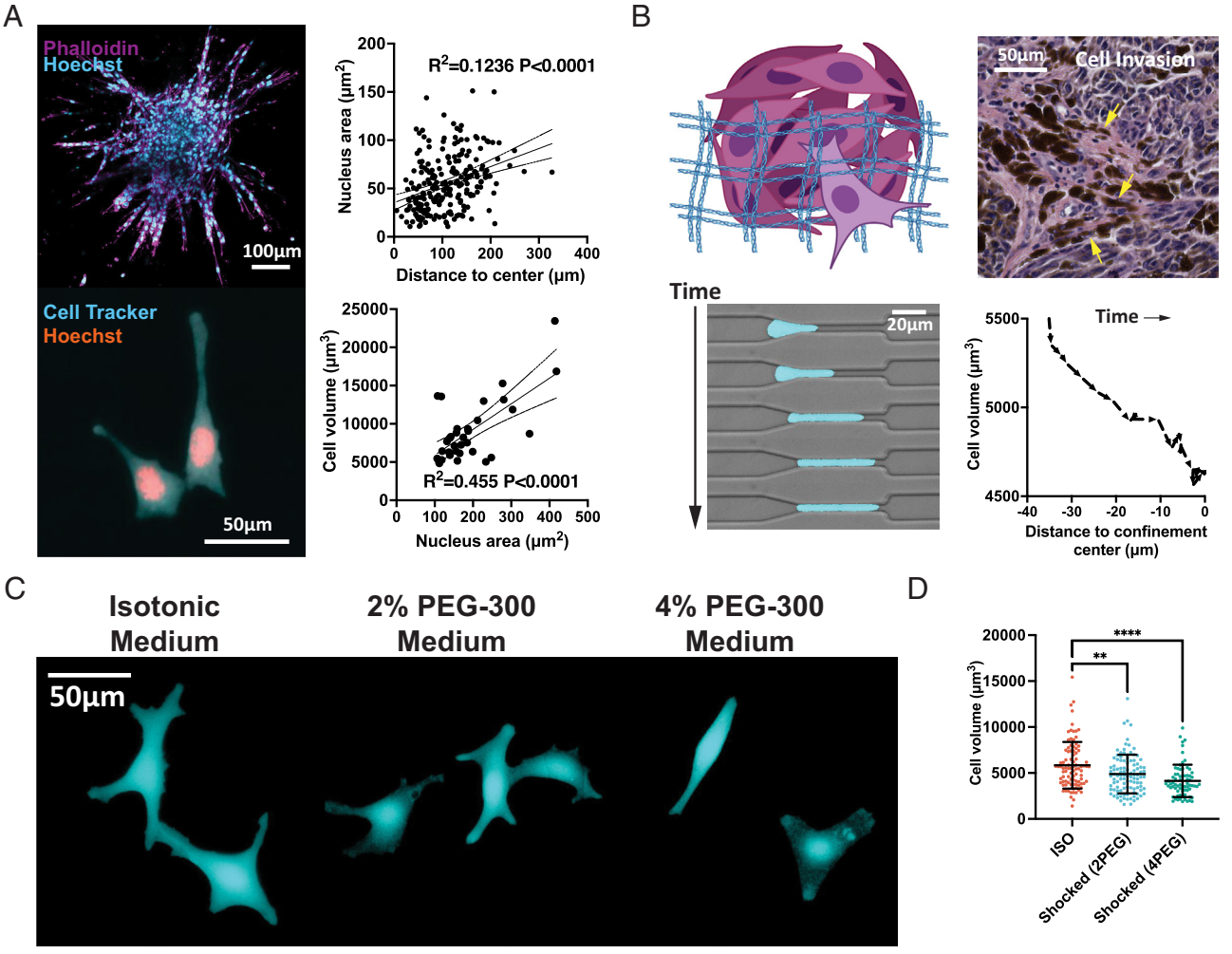

Fig. 1. Volumetric compression of melanoma during tumor progression. (*A*) *Upper*: A YUMM cell spheroid is shown in the immunofluorescent image with F-actin and nucleus stained with phalloidin and Hoechst. A linear relationship between the cell nucleus area and the cell distance to the spheroid center is plotted (n = 229, from two independent experiments). *Lower*: YUMM cells that have been grown and fixed on a 2D surface are displayed in the fluorescent image. The linear relationship between the nucleus area and cell volume of YUMM cells is plotted (n = 34, from two independent experiments). The dotted curves are 95% CIs of the linear regression. (*B*) *Upper*: Schematic of a cell invading through pores in the ECM and an image of a human melanoma biopsy sample demonstrates local tumor dissemination. *Lower*: Fluorescent images of a YUMMER cell migrating through a confined microfluidic geometry. The YUMMER cell volume decreases as the cell is compressed by the environment when entering the channel. (*C*) Confocal images of live B16F0 cells at 2 h after cultured in different medium conditions. (*D*) The volume of B16F0 cells shocked in different medium conditions is shown ($n \geq 71$ for each condition, from two independent experiments). All error bars are mean with SD. Details of statistical analyses used can be found in *Materials and Methods—Statistical Analysis*.

method has been widely used as an approach to induce volumetric compression in many biological contexts (17, 26, 33). Herein, "compression" refers to osmotically induced volumetric compression unless otherwise noted. We apply osmotic media to melanoma cells and image them 2 h after compression (Fig. 1*C*). The cell volume and 3D surface area are found to be reduced by compression in the B16F0 (Fig. 1*D* and *SI Appendix*, Fig. S1*C*), YUMM, and YUMMER (*SI Appendix*, Fig. S1*B*) melanoma cell lines. In addition, the B16F0 cells are shown to be adherent on the substrate and have reduced cell height (*SI Appendix*, Fig. S1*E*) with no changes in roundness (*SI Appendix*, Fig. S1 *F*, *a* 2D measure of how closely the shape of an object approaches that of a mathematically perfect circle, with 1 meaning perfect circle) and sphericity (*SI Appendix*, Fig. S1 *D*, *a* 3D measure of how closely the shape of an object resembles that of a perfect sphere, with 1 meaning perfect sphere) under compression, indicating that cells are not rounding up. The majority of adherent B16F0 cells were shown to be viable during 5-d compression, suggesting that the compressive stresses applied are tolerable (*SI Appendix*, Fig. S1*G*). Furthermore, the heat shock protein responses (*SI Appendix*, Fig. S8*A*) and the hypoxia-induced factor alpha subunit encoding gene Hif1a (*SI Appendix*, Fig. S8*B*) are found to be not changed in the compressed conditions. The carbonic anhydrase 9 (CAIX) encoding gene Car9 is detected to increase in the 4PEG condition (*SI Appendix*, Fig. S8*C*).

Bioinformatics Analysis of Compression-Induced Transcriptomic Adaptations. The duration of compression applied to melanoma cells could be substantially longer than a few hours in physiological and pathological cases. Previous research has suggested that 5 d is a sufficient amount of time to induce phenotypic changes and altered tumorigenicity in the B16F0 cells (6). Therefore, we design an experimental procedure to track the short- and long-term phenotypic and transcriptomic changes in B16F0 cells. Briefly, the isotonic media cultured uncompressed (also termed as ISO) cells are seeded on a 2D substrate on day -1. After overnight incubation, the media are replaced with osmotic media in varied PEG-300 concentrations (2% and 4%) to start the hypertonic culture (day 0). To determine the optimal PEG-300 concentration for our compression experiments, we leverage previous findings showing that cells located at the core of tumor organoids had a volume reduction of approximately 30% when compared to cells at the periphery of the tumor (8). The magnitude of volumetric reduction induced by the addition of 2% and 4% PEG-300 in our study (Fig. 1*D*) is similar to that observed under physiological conditions.

We annotate cells at various experimental stages to simplify future references. 1) The term "Shocked (2PEG/4PEG) cells" refers to initially uncompressed cells that have been cultured for 2 h under osmotic pressure. 2) The term "2PEG/4PEG" or "Compressed" refers to cells that have been osmotically compressed with different concentrations of PEG-300 for 5 d (Fig. 2*B*). 3) The term "Recovered (2PEG/4PEG) cells" refers to compressed cells that have been resuspended and reseeded in isotonic media for 1 d. The goal of the osmotic recovery is to access long-term sustained responses even after the compression is removed.

To investigate the association of compression-induced transcriptomic changes to melanoma patient prognosis, we conduct RNA-seq analysis and calculate the transcriptome $\log_2$ fold change between 5-d compressed and uncompressed B16F0 cells. Then, the $-\log_{10}P$ value of each gene is collected from the TCGA cutaneous melanoma dataset. The $-\log_{10}P$ (Prognosis) value is obtained by further multiplying the $-\log_{10}P$ value of each gene by either 1 (overexpression improves prognosis) or −1 (underexpression improves prognosis). Transcriptomic changes are highlighted based on how they affect prognosis (orange: improve prognosis; cyan: worsen prognosis) (Fig. 2*C*). We identify both prognosis-improving changes and prognosis-worsening changes in the compressed conditions. In particular, 61.5% (in 2% PEG-300 compressed cells) and 72.9% (in 4% PEG-300 compressed cells) of the highlighted genes are associated with improved prognosis, respectively.

We then perform multiple bioinformatics analyses on the RNA-seq results of the compressed vs. uncompressed B16F0 cells. The bioinformatics analyses include ranked gene ontology (GO), gene set variation analysis (GSVA) (Fig. 2 *D*–*F*), and network map of the GO biological process (*SI Appendix*, Fig. S2). In summary, we identify major compression-induced characteristics that are highlighted by the bioinformatics analyses, including proliferation inhibition, reduced cell motility, organelle stresses, and activated antioxidative responses to reactive oxygen species (ROS).

Compression-Induced Proliferation and Migration Suppression. We start by investigating the impact of compression on cell proliferation and migration. According to gene set enrichment analysis (GSEA), the G2M checkpoint and the mitotic spindle hallmarks are both down-regulated in compressed B16F0 cells (Fig. 3 *A* and *B*). Additionally, a list of genes related to the metaphase checkpoint from the MetaCore pathway analysis (*SI Appendix*, Fig. S3*A*) is also found to be down-regulated in compressed B16F0 cells (*SI Appendix*, Fig. S3*E*). The TCGA dataset reveals that downregulation of this gene signature is associated with an improved prognosis for cutaneous melanoma (Fig. 3*F* and *SI Appendix*, Fig. S3*B*). To validate the bioinformatics analysis, we first track the cell number over the 5-d culture and detected that cell proliferation is inhibited by compression (~threefolds for 4PEG at day 5) (Fig. 3*C*). We then verify the reduced proliferation using an EdU proliferation assay on 5-d compressed B16F0 cells (Fig. 3*D*).

Furthermore, our results demonstrate a significant reduction in cell motility-related gene ontology terms under compressed conditions, indicating suppression of migratory phenotypes (Fig. 2 *E*, *Left*). It has been reported previously that cells at the core of tumors exhibit reduced size and slower migration. This observation is suggested to be caused by the suppression of supracellular fluid flow through gap junctions, leading to delayed invasive phenotype transition (8). Our results provide transcriptomic evidence to demonstrate the inhibitory effect of compression on cell motility. To further investigate the long-term effects of compression on cell migratory phenotypes, we conduct a wound healing assay to measure the migration of recovered B16F0 cells (i.e., cells after compression for 5 d and recovered in isotonic media for 1 d) after the removal of external stress. Our results reveal persistent inhibitory effects on migratory phenotype even after the removal of external stress, suggesting that the impact of compression on cell migration is enduring (Fig. 3 *G* and *H*).

Reductions in Cytoplasmic Macromolecular Crowding and Nuclear Translocation of Transcription Factors After Recovery from Compression. It has been reported previously that tumor cell proliferation and migration can be affected by the Wnt/β-catenin and YAP/TAZ transcriptional factors (34–36). To investigate long-term sustained responses of these markers after the cells are compressed, we label β-catenin and YAP/TAZ of the recovered cells (Fig. 4 *A* and *D*) and quantify the intensity of their signal in the cytoplasm and nucleus (*SI Appendix*, Fig. S4). Both β-catenin and YAP/TAZ mean fluorescence intensity (MFI) are found reduced inside the cytoplasm (Fig. 4 *B* and *E*), indicating reduced cytoplasmic macromolecular crowding. Despite the observed reduction in MFI

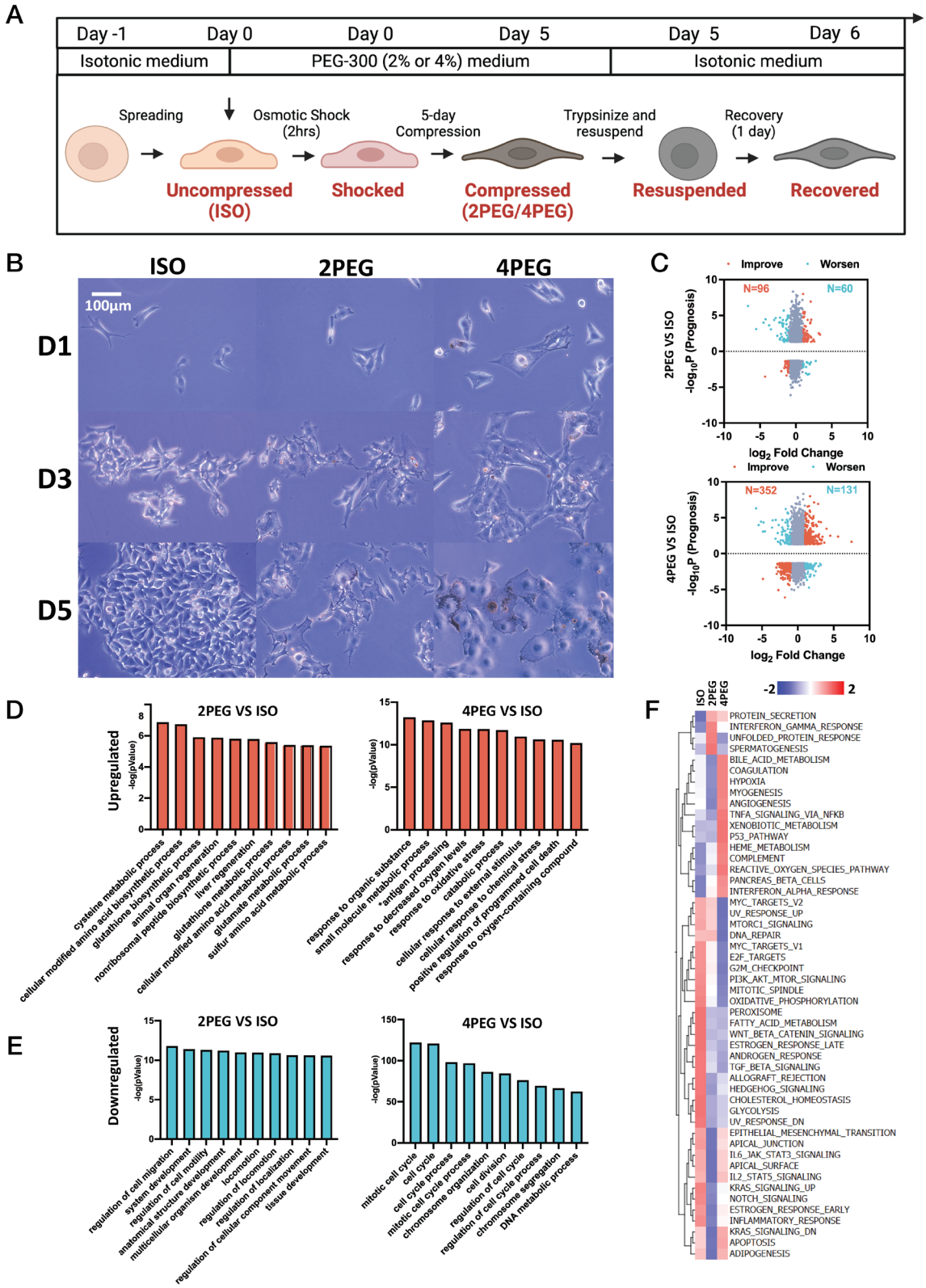

Fig. 2. Bioinformatics analysis of compression-induced transcriptomic adaptations. (*A*) Schematic showing how the osmotic medium was switched throughout the experiment. (*B*) The images of B16F0 cells cultured in different medium conditions during the 5 d are shown. (*C*) The genes' $-\log_{10}P$ (Prognosis) values from the TCGA cutaneous melanoma dataset and their $\log_2$ fold change between 5-d compressed and uncompressed B16F0 cells. *P* values were calculated using the "survdiff" R package. For genes whose overexpression that have a negative impact on prognosis, their $-\log_{10}P$ value will be multiplied by −1 to flip the gene to the negative side of the *y*-axis. Cutoff of abs(*P*) < 0.05 and abs($\log_2$ Fold Change) > 1 were applied. The genes are colored according to whether their changes detected in the compressed conditions are associated with improvement (orange) or worsening (cyan) of the patient's prognosis. (*D* and *E*) The top 10 ranked GO terms that are up-regulated (*D*) or down-regulated (*E*) in the compressed B16F0 cells are plotted. (*F*) GSVA hallmarks analysis of the uncompressed and compressed B16F0 cells is shown.

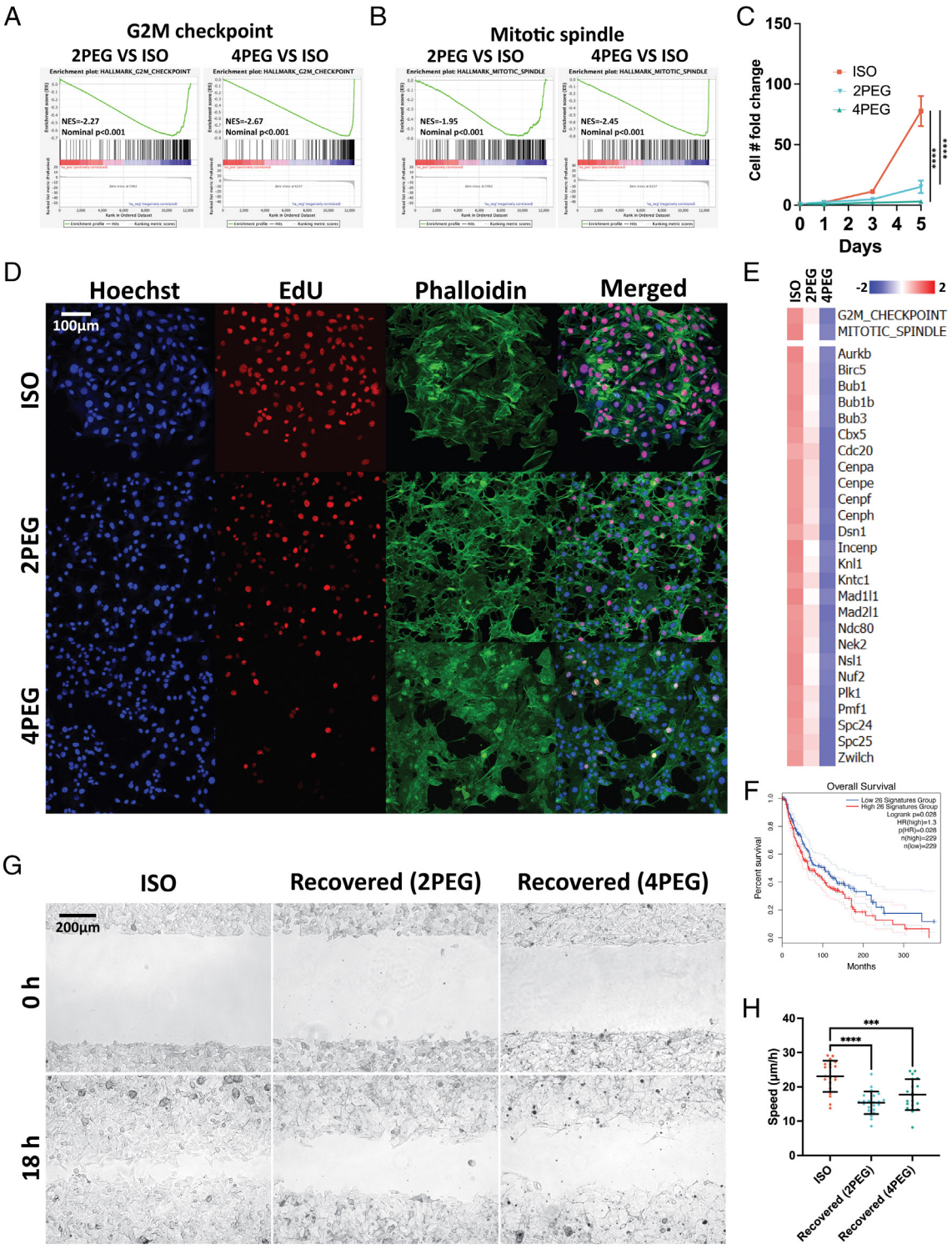

Fig. 3. Compression-induced proliferation and migration suppression. (*A* and *B*) The suppression of the G2M checkpoint (*A*) and mitotic spindle (*B*) hallmarks in the 5-d compressed B16F0 cells are shown in the GSEA plots. (*C*) The curves indicate B16F0 cell proliferation under each medium condition over the 5 d (~threefolds for 4PEG at day 5) ($n \geq 6$ wells for each condition, from three independent experiments). (*D*) Immunofluorescent images of the uncompressed and 5-d compressed B16F0 cells. (*E*) GSVA (*Upper*) and gene expression (*Lower*) analyses of the uncompressed and 5-d compressed B16F0 cells identify hallmarks or transcripts associated with cell proliferation. (*F*) The listed genes in (*E*) are grouped as a signature to separate melanoma patients in the TCGA cutaneous melanoma prognosis dataset. (*G*) Representative images of the wound area of uncompressed and recovered B16F0 cells. The images are taken at 0 and 18 h after the wound was created. (*H*) The wound healing speed of conditions in (*G*) is plotted ($n \geq 19$ wells for each condition, from three independent experiments). Error bars in (*C*) are mean with SEM, all other error bars are mean with SD. Details of statistical analyses used can be found in *Materials and Methods—Statistical Analysis*.

in the cytoplasm, the significant increase in cell spreading, which is mainly made of cytoplasm (*SI Appendix*, Fig. S5), results in a higher cytoplasmic sum fluorescence intensity (SFI) of β-catenin and YAP/TAZ. As a consequence, the translocation of β-catenin and YAP/TAZ to the nucleus (relative to the total amount of each) is found to be reduced in the recovered cells (Fig. 4 *C* and *F*). This evidence suggests long-term modifications in mechanotransduction pathways, even after the removal of external compression.

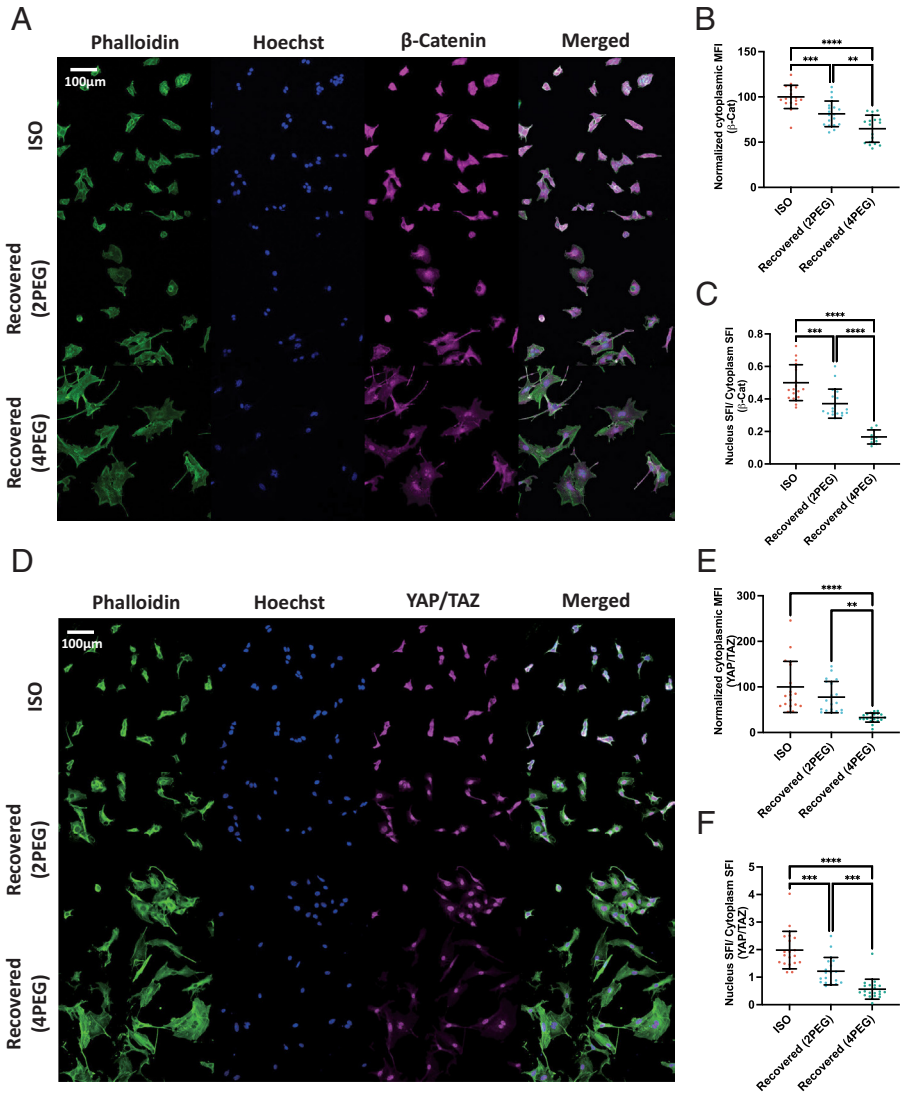

Fig. 4. Reductions in cytoplasmic macromolecular crowding and nuclear translocation of transcription factors after recovery from compression. (*A*) Immunofluorescent images of uncompressed and recovered B16F0 cells. (*B*) The normalized cytoplasmic mean fluorescence intensity (MFI) of β-catenin is shown in the scatter plots ($n \geq 18$ wells for each condition, from two independent experiments). (*C*) The percentage of translocated β-catenin inside the nucleus is shown in the scatter plots ($n \geq 12$ wells for each condition, from two independent experiments). (*D*) Immunofluorescent images of uncompressed and recovered B16F0 cells. (*E*) The normalized cytoplasmic MFI of YAP/TAZ is shown in the scatter plots ($n \geq 18$ wells for each condition, from two independent experiments). (*F*) The percentage of translocated YAP/TAZ inside the nucleus is shown in the scatter plots ($n \geq 12$ wells for each condition, from two independent experiments). All error bars are mean with SD. Details of statistical analyses used can be found in *Materials and Methods—Statistical Analysis*.

Compression-Induced Intracellular Organelle Stress. To address the organelle state of the cells, we first investigate the endoplasmic reticulum (ER) response in the compressed B16F0 cells. The GSEA analysis indicates that compressed cells have activated misfolded protein binding, ER unfolded protein response, and regulation of response to ER stress pathways (Fig. 5*A*). Next, we investigate the mitochondria of shocked B16F0 cells. The mitochondria of cells are labeled with tetramethylrhodamine, methyl ester (TMRM), a mitochondria membrane potential marker to indicate functional mitochondria (37) (Fig. 5*B*). The analysis of 3D mitochondria TMRM images suggests that compression reduces the total volume of functional mitochondria (Fig. 5 *C*, *Upper*), indicating that compression impairs cell mitochondria function. Furthermore, the quantification of functional mitochondria clusters (regions of interconnected mitochondria segmented from 2d slides) from the binarized images suggests that compression shock reduces functional mitochondria cluster size (Fig. 5 *C*, *Lower*). Last, we access the nucleus condition of the recovered B16F0 cells and detect an increased percentage of cells with nuclear envelope rupture in recovered cells (Fig. 5*E*). Overall, we demonstrate that compression can induce a variety of intracellular organelle stresses at different time points.

Compression-Induced Pigmentation in Multiple Cell Lines and in a Variety of Physical and Environmental Contexts. One notable phenotypic adaptation found in compressed cells is cell pigmentation (Fig. 6 *A*–*D*). Using the melanin assay, we show that compressed cells contain more melanin (Fig. 6 *E*, *Left*). To produce high-throughput live-cell melanin quantification measures, we analyze the bright-field images, extract the brightness channel, and binarize the resulting images to highlight melanin regions (Fig. 6*B*). The binarized melanin area percentage in the field of view (FOV) (Fig. 6 *E*, *Right*) quantifies melanin at comparable levels to the standard melanin assay (Fig. 6*F*), and it also correlates with the mean brightness of the FOVs (Fig. 6*G*). In addition to the mouse melanoma B16F0 and B16F10 cell lines, we further apply compression on the YUSIK human melanoma cell line (38) and primary human melanocytes. We demonstrate that various human and mouse melanoma cells as well as normal melanocytes exhibit compression-induced pigmentation (Fig. 6*C* and *SI Appendix*, Fig. S6*A*).

To prove that compression-induced pigmentation can also be induced mechanically (in addition to osmotically), we compress cells mechanically using a transwell piston setup similar to the one used in a previous study (39). Briefly, the experimental setup is as follows: 1) Cells are cultured to form a monolayer on the upper side of the transwell's transmembrane. The insert is soaked into a well with culture media to allow media exchange during culture. 2) An agarose cushion is then used to cover the cell monolayer to provide more uniform pressure and a piston holder is then applied on top of the agarose cushion. 3) Beads with the desired amount of weight are gradually put inside the holder to apply vertical forces to the cell

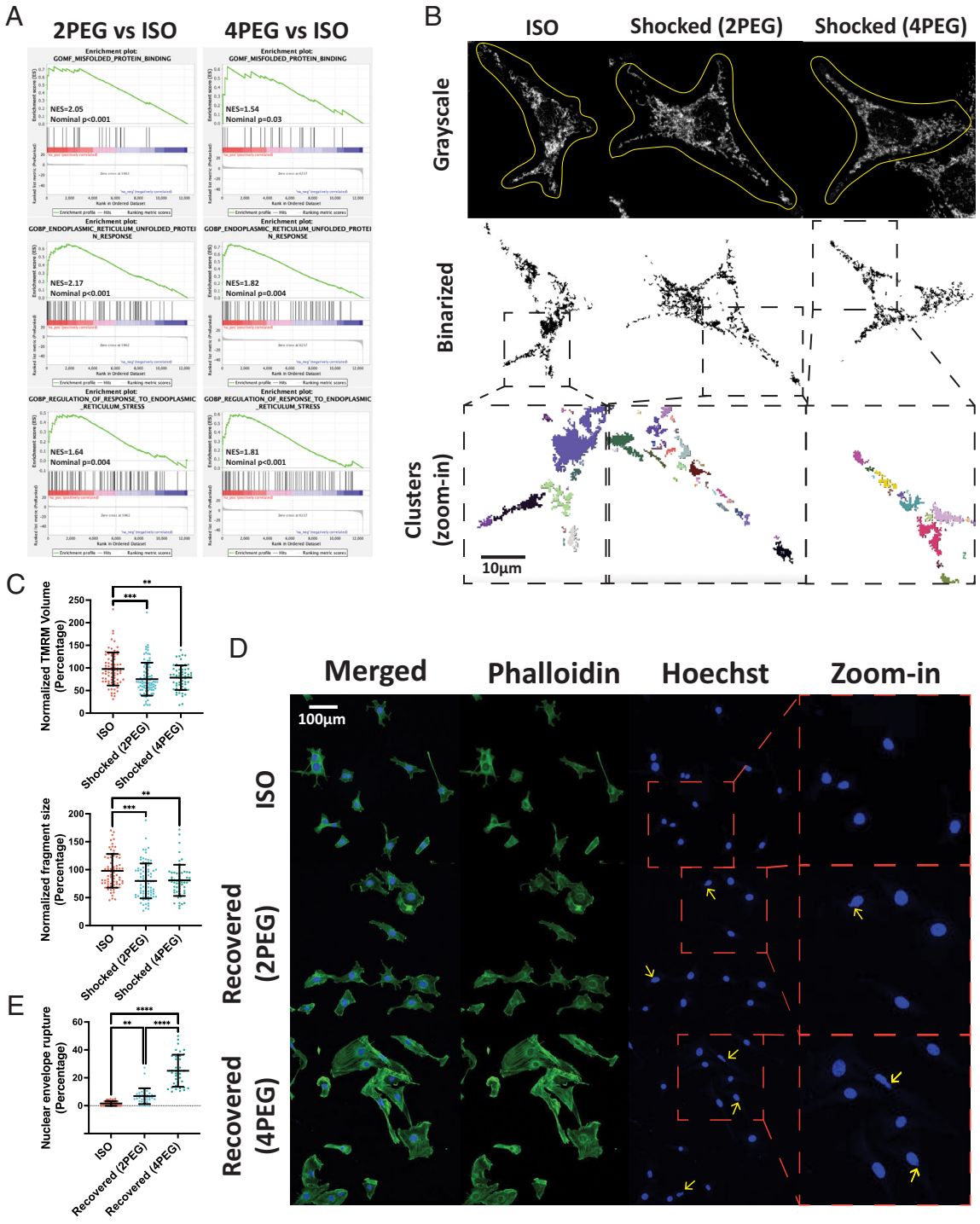

Fig. 5. Compression-induced intracellular organelle stress. (*A*) The activation of the misfolded protein binding, ER unfolded protein response, and regulation of response to ER stress in the 5-d compressed B16F0 cells are shown in the GSEA plots. (*B*) The grayscale (*Upper*) images with manually drawn cell contours, the binarized images (*Middle*), and the color-coded zoom-in individual cluster (*Lower*) images of representative uncompressed and shocked B16F0 cells are shown. The mitochondria left outside the contours are from other cells. (*C*) The mitochondria-related characteristics in the uncompressed and shocked B16F0 cells are compared in the scatter plots ($n \geq 59$ for each condition, from two independent experiments). (*D*) Immunofluorescent images of recovered B16F0 cells. Yellow arrows indicate nuclear envelope rupture. (*E*) The percentage of cells with a nuclear envelope rupture in each condition is shown ($n = 37$ wells for each condition, from four independent experiments). All error bars are mean with SD. Details of statistical analyses used can be found in *Materials and Methods—Statistical Analysis*.

monolayer and a lid is used to cover the sample from being exposed to the environment. The outcomes indicate that the B16F0 cells start to pigment 2 d after being mechanically compressed (Fig. 6*H*). We show that cells undergo similar pigmentation phenotypes in both mechanical and osmotic compression conditions (Fig. 6*B*).

Additionally, we embed B16F0 cells into a 3D collagen gel, and the cells are compressed via osmotic media (Fig. 6 *I*, *Left*). After undergoing a 7-d osmotic compression period, the in-focus spheroids are manually circled and their respective areas and brightness are quantified. Results indicate a significant reduction in the spheroid area as well as decreased spheroid brightness in the compressed conditions (Fig. 6 *I*, *Right*).

Finally, we image a biopsy sample of human melanoma. The brightness channel is extracted from the brightfield image. The

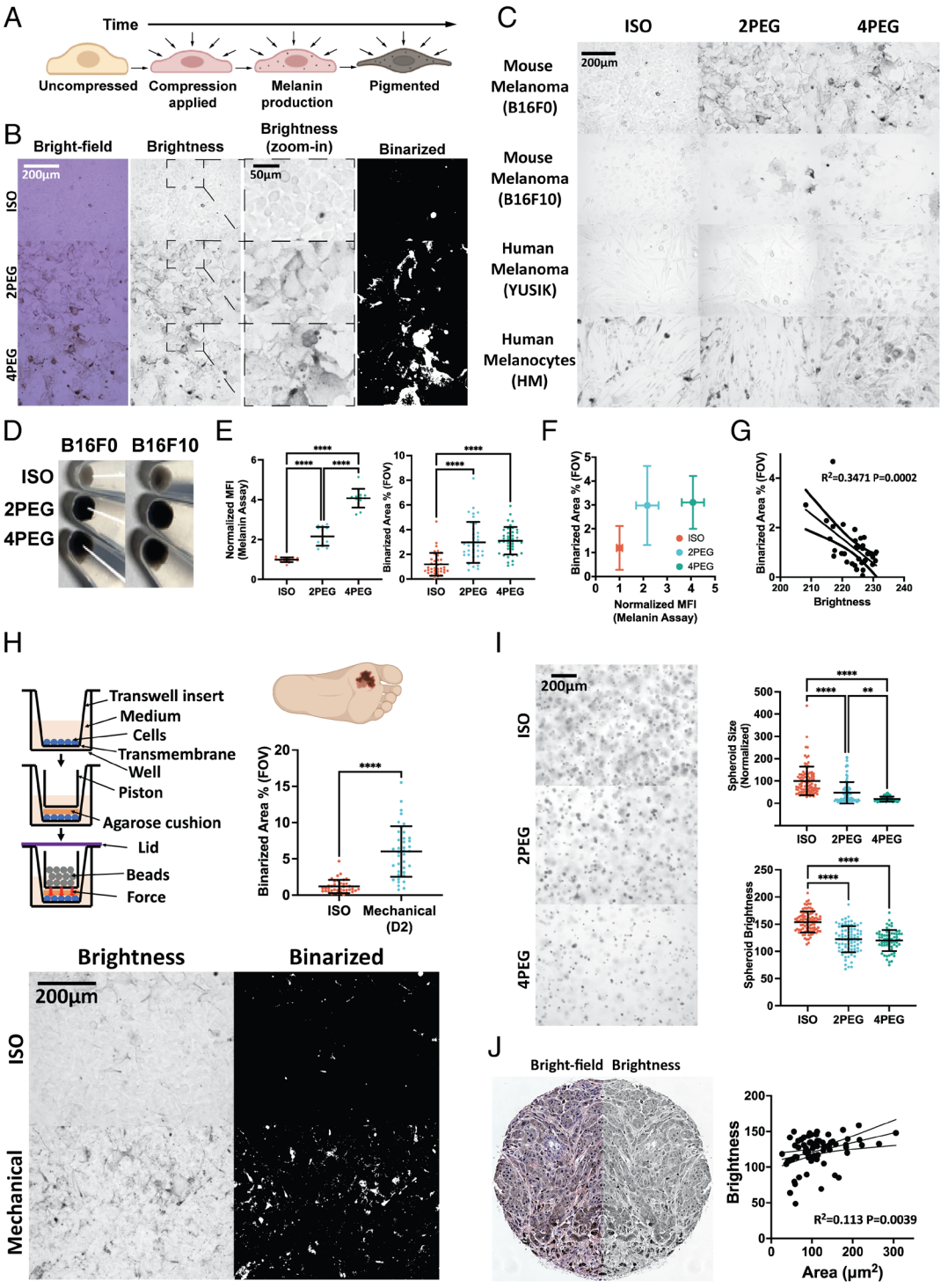

Fig. 6. Compression-induced pigmentation in multiple cell lines and in a variety of physical and environmental contexts. (*A*) Schematic showing a gradual pigmentation through the production of melanin in cells under compression. (*B*) Brightfield, brightness, zoom-in brightness, and zoom-in binarized images of uncompressed and 5-d compressed B16F0 cells. (*C*) Images of multiple cell lines compressed for 5 d. (*D*) Images of the uncompressed and 5-d compressed cell pellets (500 k/vial). (*E*) Melanin assay MFI (*Left*) and binarized melanin area percentage (*Right*) of the uncompressed and 5-d compressed B16F0 cells are plotted (n = 13 for each condition in the melanin assay plot, from two independent experiments. $n \geq 37$ for each condition in the binarized area percentage plot, from three independent experiments). (*F*) The plot displays the association between the melanin assay and the binarized melanin area percentage in (*E*). (*G*) The scatter plot displays a linear relationship between the FOV mean brightness and the binarized melanin area percentage of uncompressed B16F0 cells (n = 34, from two independent experiments). The dotted curves are 95% CIs of the linear regression. (*H*) *Upper-left*: Schematic of a transwell piston setup. *Bottom*: Images of B16F0 cells with or without 2 d of mechanical (6.25 g weight on 176.71 mm^2 contact area) compression. The plot displays the binarized melanin area percentage between the mechanical compressed and uncompressed conditions ($n \geq 38$ for each condition, from three independent experiments). (*I*) *Left*: Images of uncompressed and 7-d compressed B16F0 cells in collagen gels. *Right*: The spheroid size (normalized) and spheroid brightness in each condition are presented ($n \geq 68$ for each condition, from two independent experiments). (*J*) Images show a representative human melanoma biopsy sample's brightfield (*Left*) and its mirrored brightness (*Right*) channels. The scatter plot demonstrates a linear relationship between cell area and brightness (n = 72). All error bars are mean with SD. Details of statistical analyses used can be found in *Materials and Methods—Statistical Analysis*.

single-cell area is manually circled and cell brightness is measured. We demonstrate that cells with smaller cell areas are darker (indicated by lower brightness) (Fig. 6*J*).

Compression-Induced Pigmentation is Affected by Increased Oxidative Stress. We then investigate antioxidant defense mechanisms. The ROS pathway hallmark is found to be activated in compressed conditions using GSVA (Fig. 7 *A*, *Upper*) and GSEA (Fig. 7*B*) analyses. Important antioxidant defense factors such as superoxide dismutases (SODs) that transform superoxide radical (O_2^-) into hydrogen peroxide (H_2O_2), catalase (Cat) and the glutathione pathway (Gclc, Gclm, Glrx, Glrx2, Gpxs, and Gss) that further transform hydrogen peroxide into water (H_2O) and oxygen (O_2), are shown to be activated (40) (Fig. 7 *A*, *Lower*). These data suggest that cells activate antioxidative responses to compression. To test the impact of oxidative stress on cell pigmentation, we use a variety of positive controls, including H_2O_2 (41), cisplatin (42), and doxorubicin (43) that are shown to induce intracellular oxidative stresses. We demonstrate that without any external compression, pigmentation appears after 5 d (or 2 d for H_2O_2) of treatments in the ROS-positive conditions (*SI Appendix*, Fig. S6 *B–D*). The compression-induced pigmentation can be diminished when the ROS scavenger N-Acetyl Cysteine (NAC) (44, 45) is introduced into the osmotic compression and mechanical compression conditions (Fig. 7 *C* and *D*). These results further demonstrate that both osmotic compression and mechanical compression induce melanoma pigmentation in a ROS-dependent manner.

Compression-Induced Tumor Cell Chemoresistance. In addition to the adaptations shown above, the RNA-seq data of the compressed cells reveal gene expression associated with reduced drug uptake (Slc31a1) (46), higher drug efflux (ATP-binding cassette genes) (47), and activation of the glutathione pathway that has been previously shown to detoxify cisplatin's effects (48) (Fig. 8*A*). These results indicate that compression can induce transcriptomic changes that favor a cisplatin-resistant phenotype. To investigate this, after culturing cells under osmotic compression in hypertonic media for 5 d, we transfer the compressed cells back to isotonic media at the same initial seeding density and allow them to recover for 1 d. Following the 1 d of recovery, the recovered cells are treated with cisplatin for an additional 1 d. The percentage of cells that survive this treatment is quantified. The live/dead staining reveals that cells that have experienced compression have a higher survival rate from a subsequent cisplatin treatment (Fig. 8 *B* and *C* and *SI Appendix*, Fig. S7).

Discussion

As the tumor grows, melanoma cells are exposed to a variety of physical stimuli. The potential events that could lead to volumetric reduction during tumor progression include: 1) Inside the rapidly growing tumor tissue, cells can experience physical compression from neighbors (49, 50), which would lead to volumetric compression (8) (depicted in Fig. 1*A*). 2) During cancer metastasis, cells migrate through environments with cross-sectional areas ranging from 10 to >300 μm^2 (14). To facilitate migration, cells need to

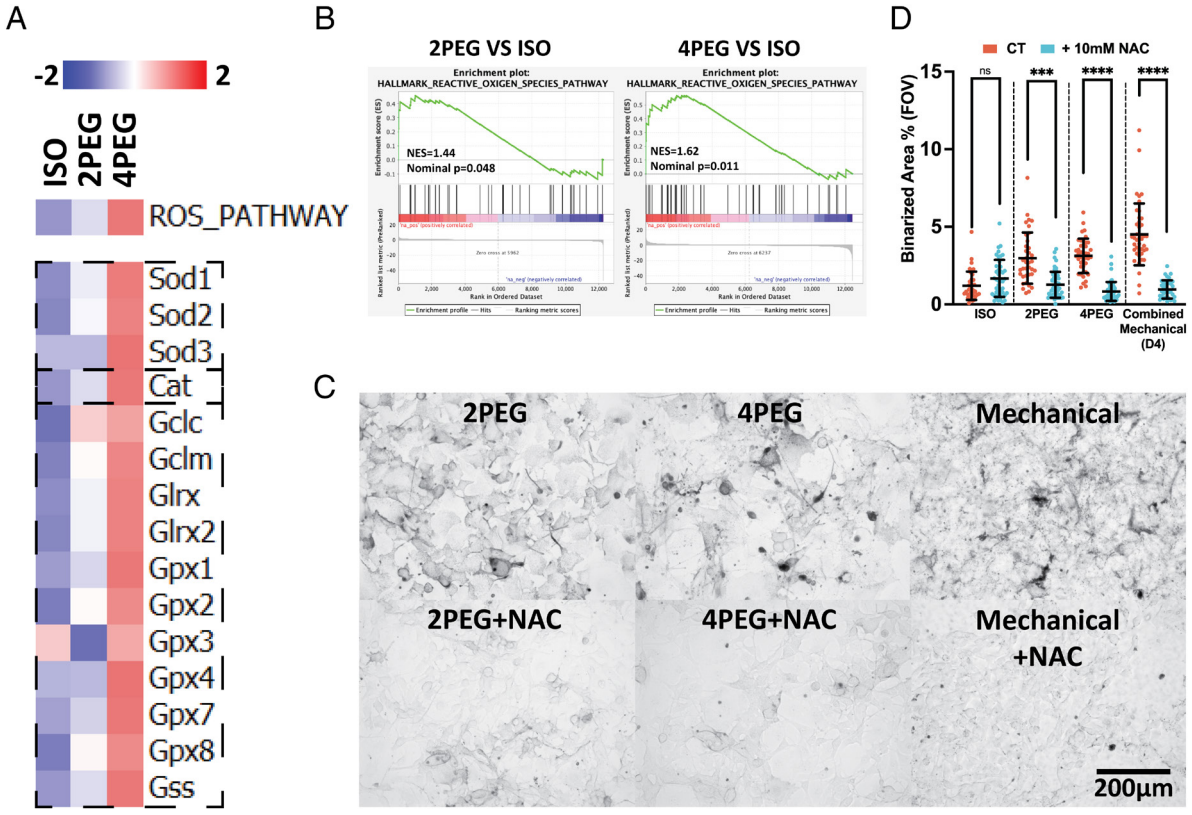

Fig. 7. Compression-induced pigmentation is affected by increased oxidative stress. (*A*) GSVA (*Upper*) and gene expression (*Lower*) analyses of the compressed B16F0 cells identified hallmarks and transcripts associated with cellular response to oxidative stress. (*B*) The activation of the ROS hallmark in the 5-d compressed B16F0 cells is shown in the GSEA plots. (*C*) *Upper*: Images of B16F0 cells cultured under osmotic or mechanical compression. *Lower*: Images of cells cultured under osmotic or mechanical compression with the addition of 10 mM NAC throughout the culture. (*D*) The scatter plot shows the percentage of binarized melanin in each B16F0 group treated with or without 10 mM NAC during the culture under osmotic (D5) or mechanical (D4, combined data of 3.16 g, 4.58 g, and 6.25 g weights on 176.71 mm^2 contact area) compression ($n \geq 34$ for each condition, from three independent experiments). All error bars are mean with SD. Details of statistical analyses used can be found in *Materials and Methods—Statistical Analysis*.

deform physically (16) and reduce volume during invasion (18), leading to volume differences of cells migrating inside confined environments vs. nonconfined environments (depicted in Fig. 1*B*). In both cases, cells would experience volumetric reduction as a result of compression (from neighbors and from the environment). These physical stressors can induce short- and long-term changes to genetic and phenotypic profiles.

To identify significant compression-induced alterations in melanoma, in particular via osmotic pressure, we conducted an integrative investigation that combines bioinformatics analyses and in vitro experiments. We performed bioinformatics analyses to thoroughly screen transcriptomic changes in compressed cells for notable characteristics (Fig. 2 *C*–*F* and *SI Appendix*, Fig. S2). Then, we conducted in vitro experiments to further verify those characteristics (Figs. 3–8). We demonstrated that compression-induced characteristics lead to counteractive impacts on melanoma progression, both inhibiting and protecting tumor cells.

We first demonstrated compression as a factor that impedes tumor progression. Tumor proliferation and migration are major hallmarks of cancer (4) regulated by multiple evolutionary mechanisms (6, 51). Elevated tumor cell proliferation and migration have been shown to correlate strongly with poor patient prognosis (52, 53). We found that compression can significantly reduce cell proliferation and migration (Fig. 3). The transcriptomic changes identified in the compressed cells are shown to be associated with improved patient prognosis in the TCGA dataset (Fig. 3 *E* and *F* and *SI Appendix*, Fig. S3*B*). In addition, the nuclear translocation of the Wnt/β-catenin and the YAP/TAZ transcriptional factors are major factors that drive tumor migration and proliferation (34–36). We identified reduced nuclear translocation and cytoplasmic macromolecular crowding in both transcriptional factors, which may also be related to the suppression of tumor progression.

We found that compression, a physical stressor, induces intracellular oxidative stress (Fig. 7) and cell pigmentation in multiple melanoma and normal human melanocyte cell lines (Fig. 6*C* and *SI Appendix*, Fig. S6*A*). Cell pigmentation is a natural response of skin cells to resist solar radiation (54), which is known to cause cellular damage and elevate intracellular ROS levels (55). The production of melanin can effectively dissipate radiation (56). Here, our study demonstrated that compression can induce pigmentation in various cell types (Fig. 6*C* and *SI Appendix*, Fig. S6*A*) using different mechanical and osmotic compression methods (Fig. 6 *H* and *I*). We first validated that cell pigmentation can be induced through the addition of known ROS inducers such as H_2O_2 (41), cisplatin (42), and doxorubicin (43) (*SI Appendix*, Fig. S6 *B*–*D*) into the culture medium of uncompressed cells. Next, we showed that the elimination of ROS using the ROS scavenger NAC (44, 45) can prevent cells from pigmenting in both mechanical and osmotic compression (Fig. 7 *C* and *D*). This evidence suggests that compression-induced pigmentation is ROS-dependent. Our next step was to understand how intracellular oxidative stresses are generated by compression. It has been suggested that organelle stresses, such as ER stress and mitochondrial dysfunction, are the major sources of intracellular ROS production (57, 58). We investigated the condition of cell organelles and showed that compression can induce a series of organelle stresses, such as ER unfolded protein response (Fig. 5*A*), reduced functional mitochondria (Fig. 5 *B* and *C*), and nucleus envelope rupture (Fig. 5 *D* and *E*). Overall, our findings suggested that cells experience organelle and oxidative stresses under compression.

Remarkably, our study has unveiled compression as a crucial physical factor that propels tumor cell resistance against chemotherapy. A series of cellular adaptations including impaired membrane transport of drugs and increased cytoplasmic detoxification are shown to potentially confer cancer resistance to chemotherapy (48). Tumor progression can introduce various compression-related scenarios. To investigate the effect of compression on chemoresistance, we compared transcriptomic data from compressed and uncompressed cells. We identified several chemoresistance-related

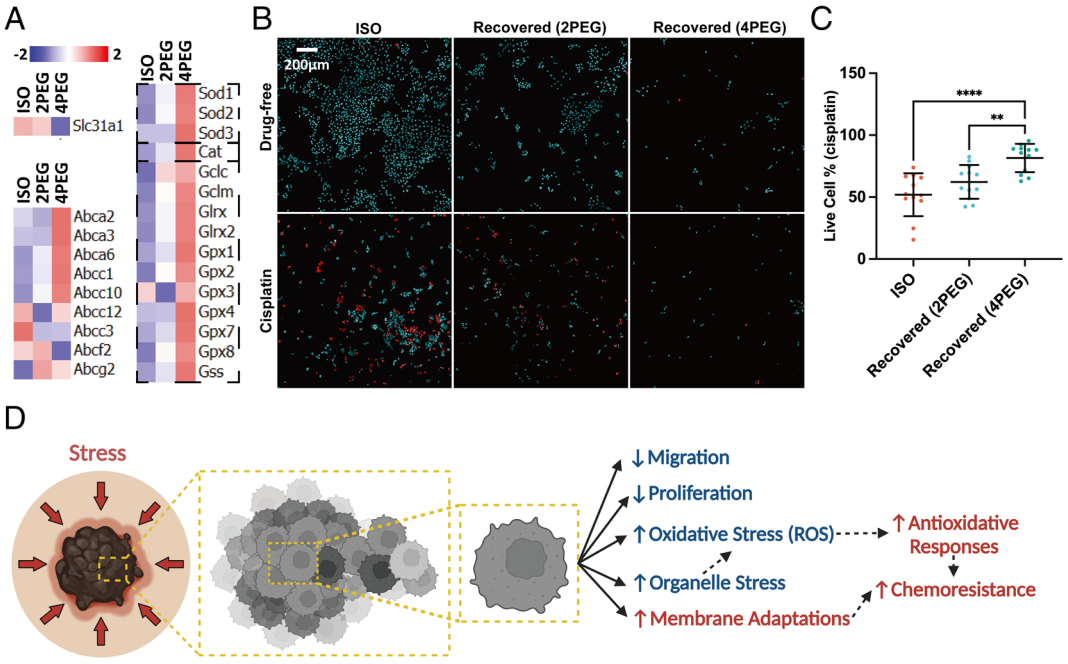

Fig. 8. Compression-induced tumor cell chemoresistance. (*A*) Gene expression analyses of the 5-d compressed B16F0 cells identify transcripts associated with cell chemoresistance. (*B*) A 3 × 2 panel of images showing a total of six different conditions from separate wells. Each image is a 3 × 3 tile scan that is autostitched via Leica LASX software. The images of live/dead staining of recovered B16F0 cells treated with (*Lower*) or without (*Upper*) 110 μM cisplatin for 1 d. The dead cells are colored red. (*C*) The percentage of survived cells in the uncompressed and recovered conditions after 1 d of cisplatin treatment is plotted (n = 12 wells for each condition, from three independent experiments). (*D*) A working hypothesis on compression-induced melanoma evolutions. All error bars are mean with SD. Details of statistical analyses used can be found in *Materials and Methods—Statistical Analysis*.

genes expressed in compressed cells. Specifically, we detected decreased expression of the Slc31a1 gene (Fig. 8*A*). The copper transporter-1 (CTR1) encoded by Slc31a1 was suggested to have key responsibility for cisplatin influx (59). Loss of CTR1 function can significantly increase drug resistance by impairing the uptake of platinum drugs in cancer cells (60). We detected activation of several major genes within the ATP-binding cassette (ABC) transporter family (Fig. 8*A*), which are known to contribute to chemoresistance by reducing the intracellular accumulation of chemotherapy drugs (61). We also observed the activation of glutathione-related genes (Fig. 8*A*). Glutathione can conjugate cisplatin and enhance its export from cells, resulting in cytoplasmic detoxification (48). Additionally, cisplatin has been shown to induce mitochondrial ROS and mitochondria-mediated apoptosis (42). Our data suggested that the antioxidative responses (Fig. 7 *A* and *B*) induced by an earlier compression may further prevent the accumulation of subsequent cisplatin-induced ROS and facilitate chemoresistance. To confirm the effect of compression-induced chemoresistance, we exposed recovered cells (i.e., cells compressed for 5 d and recovered in isotonic media for 1 d) to cisplatin and found that compressed cells showed higher survival rates (Fig. 8 *B* and *C*). Together, our findings provided evidence that compression can drive chemoresistance in tumor cells.

Overall, we demonstrated that volumetric compression plays a double-edged sword role in melanoma progression (Fig. 8*D*). On the one hand, compression inhibits the proliferation and migration of melanoma cells, thereby suppressing tumor progression. Compression also leads to subcellular activities such as ER stress, reduced mitochondria function, and nuclear envelope rupture, which contribute to elevated intracellular organelle stress and oxidative stress. On the other hand, compression drives transcriptomic activities such as membrane transporter adaptations, antioxidant responses, and cytoplasmic detoxifications that promote the survival of tumor cells from chemotherapy. Our study elucidated how melanoma cells change in response to physical stress, which may serve as a mechanism of selection to shape the evolution of tumor cell populations. The present study focuses on the impact of volumetric compression, particularly triggered via hyperosmotic stress, as a physical stimulus on inducing cell state adaptations. Further exploration into the potential for similar adaptations resulting from other forms of compression (e.g., confined environments) across varying time scales presents interesting future directions.

Materials and Methods

Histology and Cell Lines. The histology microarray was acquired from the Department of Pathology at Yale University. B16F0 and B16F10 mouse melanoma cells were purchased from American Type Culture Collection (ATCC). YUMM and YUMMER cells were gifts from the Bosenberg lab at Yale. Human melanoma YUSIK cell line and normal human melanocytes were gifts from the Halaban lab at Yale.

B16F0: A mouse melanoma cell line obtained from the skin tissue of a melanoma-affected mouse, which comprises a combination of spindle-shaped and epithelial-like cells.

B16F10: A mouse melanoma cell line obtained from the skin tissue of a melanoma-affected mouse, which comprises a combination of spindle-shaped and epithelial-like cells.

YUMM: Yale University Mouse Melanoma cells, epithelial-like cells obtained from the skin of an adult male mouse with melanoma, from Yale University's mouse melanoma cells collection.

YUMMER: YUMM Exposed to Radiation, a cell line derived from YUMM after being exposed to multiple rounds of UV irradiation.

YUSIK: A cutaneous melanoma cell line obtained from a female human lymph node. It is part of Yale University's melanoma cell collection.

HM: Human melanocytes obtained from a newborn's foreskin.

Cell Culturing

B16F0 and B16F10 cells were passaged in Dulbecco's Modified Eagle Medium (DMEM) with 10% fetal bovine serum (FBS) and 1% penicillin-streptomycin. YUMM and YUMMER cells were passaged in DMEM/F12 with 10% FBS and 1% penicillin–streptomycin. The primary human melanoma was passaged in OptiMEM with 5% FBS and 1% penicillin–streptomycin. The normal human melanocytes were passaged in OptiMEM with 5% FBS, 1% penicillin–streptomycin, 10 ng/ml bFGF, 1 ng/ml Heparin, 0.1 mM dbcAMP, and 10 μM IBMX. The media were changed every 2 to 3 d. The cells were split every 3 to 4 d. All cells were cultured in an incubator at 37 °C with 5% CO_2.

Osmotic Medium Preparation and Culture. Isotonic culture medium was mixed with either 2 % (2PEG) or 4 % (4PEG) PEG-300 to create the osmotic medium. The Wescor EliTech Vapro 5600 Vapor Pressure Osmometer was used to measure medium osmolality. As illustrated in Fig. 2*A*, 1 d before osmotic compression, the desired number of cells (adjusted initial seeding density so cells in each condition reach ~80% confluence at day 5) was seeded in an isotonic medium. The isotonic medium was subsequently changed by an osmotic medium the next day of cell seeding. The cells were cultured under the osmotic medium for 5 d. The medium was refreshed every 2 to 3 d.

Microscope and Fluorescent Imaging. The histology microarray was imaged using an EVOS™ M7000 Imaging System (Invitrogen™). The brightfield images were taken by a Leica DMi1 with a 20× objective. Fluorescent images were taken by a confocal laser scanning microscope (Leica TCS SP8) with either a 63× (Fig. 1*A* single cell, Figs. 1 *C* and 5 *B*), 40× (Fig. 1*A* spheroid), or 20× (Figs. 1*B*, 3*D*, 4 *A* and *D*, 5*D*, 8*B* and *SI Appendix*, Figs. S1*G* and S5*A*) objective. The Z-step was set to be 0.3 μm (Fig. 1*A* single cell, Figs. 1*C* and 5*B*), 0.5 μm (Figs. 4 *A* and *D* and 5*D* and *SI Appendix*, Fig. S5*A*), or 1 μm (Fig. 1*A* spheroid, Figs. 1*B*, 3*D* and 8*B* and *SI Appendix*, Fig. S1*G*). Imaris or custom ImageJ scripts were used to process the fluorescence and microscope images.

RNA-seq and Bioinformatics Analyses. The RNeasy Micro Kit (Qiagen, Germany) was used to extract total RNA from the lysed cells, and the RNA was then sequenced at the Yale Center for Genome Analysis. Two independent experiments and sequencing were conducted. The RNAseq fastq data were mapped to the mouse genome (GRCm38) with STAR (2.7.9a) 2-pass mode. Then, the mapping result is indexed by samtools (1.11). HTSeq (0.13.5) was applied to summarize gene counts. Custom scripts (built-in Perl v5.16.3 and R v3.4.1) were used to analyze, organize the data, and get the expression matrix. The expression matrix is analyzed in R (v4.1.3). Differential expression analysis was performed with DESeq2 (1.18.1). Then, clusterProfiler (v4.2.2) and org.Mm.eg.db (v3.14.0) were used to translate biological IDs. The metric used in GSEA is $-\log_{10}$ (*P* value) and signs were added on the metric based on fold-change direction. GSVA analysis was performed with custom scripts. MetaCore was used to generate pathway maps and GO rankings. The Broad Institute's GSEA software (4.2.3) was used to produce GSEA graphs. The network map was created with Cytoscape based on the GSEA output of the GO analysis.

Statistical Analysis. The n numbers shown in the figure legend represent the total sample size. A one-way ANOVA with a Tukey post hoc test was used for the multigroup comparisons shown in Figs. 1*D*, 3 *C* and *H*, 4 *B*, *C*, *E*, and *F*, 5 *C* and *E*, 6 *E* and *I*, and 8*C* and *SI Appendix*, Figs. S1 *C–G*, S5 *B* and *C*, and S6*A*

(conditions in the B16F10, YUSIK, and HM group are compared separately), *SI Appendix*, Fig. S6 *C* and *D* (only statistics between each treatment condition and the control condition were plotted), and *SI Appendix*, Fig. S8 *B* and *C*. An unpaired *t* test was applied to analyze the two-group comparisons in Figs. 6*H* and 7*D* (conditions in the ISO, 2PEG, 4PEG and Mechanical group are compared separately), *SI Appendix*, Fig. S7 (conditions in the ISO, recovered 2PEG are recovered 4PEG group are compared separately). The nominal *P* value of all GSEA plots in Figs. 3 *A* and *B*, 5*A*, 7*B*, and *SI Appendix*, Fig. S8*A* was calculated based on a previous study (62). The *P* value of the survival comparisons shown in Figs. 2*C* and 3*F* and *SI Appendix*, Fig. S3*B* was calculated using the Kaplan–Meier estimate. $^{*}P < 0.05$; $^{**}P < 0.01$; $^{***}P < 0.001$; and $^{****}P < 0.0001$ were used to indicate statistical significance.

Data, Materials, and Software Availability. All other study data are included in the article and/or *SI Appendix*. The raw sequencing data have been uploaded to National Center for Biotechnology Information Sequence Read Archive (Bioproject ID: PRJNA982577) (63).

ACKNOWLEDGMENTS. We acknowledge support from NIH grants R01CA216101 and R35GM142875 to M.M.X.Z. was funded in part by the Yale University Frederic Ewing Fellowship. We acknowledge Dr. Gerald Shadel for helpful discussions. We acknowledge Dr. Rong Fan and Dr. Yanxiang Deng for their support with the bioinformatics analysis and access to the EVOS™ M7000 Imaging System (Invitrogen™). We acknowledge Wanshu Wang for providing support with the graphical design.

1. T. R. Gregory, T. Ryan Gregory, Understanding natural selection: Essential concepts and common misconceptions. *Evolution* **2**, 156–175 (2009).
2. A. A. Alizadeh *et al.*, Toward understanding and exploiting tumor heterogeneity. *Nat. Med.* **21**, 846–853 (2015).
3. C. E. Meacham, S. J. Morrison, Tumour heterogeneity and cancer cell plasticity. *Nature* **501**, 328–337 (2013).
4. D. Hanahan, R. A. Weinberg, Hallmarks of cancer: The next generation. *Cell* **144**, 646–674 (2011).
5. H. Easwaran, H.-C. Tsai, S. B. Baylin, Cancer epigenetics: Tumor heterogeneity, plasticity of stem-like states, and drug resistance. *Mol. Cell* **54**, 716–727 (2014).
6. J. Lee, A. A. Abdeen, K. L. Wycislo, T. M. Fan, K. A. Kilian, Interfacial geometry dictates cancer cell tumorigenicity. *Nat. Mater.* **15**, 856–862 (2016).
7. S. M. Shaffer *et al.*, Rare cell variability and drug-induced reprogramming as a mode of cancer drug resistance. *Nature* **546**, 431–435 (2017).
8. Y. L. Han *et al.*, Cell swelling, softening and invasion in a three-dimensional breast cancer model. *Nat. Phys.* **16**, 101–108 (2020).
9. R. K. Jain, J. D. Martin, T. Stylianopoulos, The role of mechanical forces in tumor growth and therapy. *Annu. Rev. Biomed. Eng.* **16**, 321–346 (2014).
10. G. Helmlinger, P. A. Netti, H. C. Lichtenbeld, R. J. Melder, R. K. Jain, Solid stress inhibits the growth of multicellular tumor spheroids. *Nat. Biotechnol.* **15**, 778–783 (1997).
11. T. Stylianopoulos *et al.*, Causes, consequences, and remedies for growth-induced solid stress in murine and human tumors. *Proc. Natl. Acad. Sci. U.S.A.* **109**, 15101–15108 (2012).
12. V. K. Gupta, O. Chaudhuri, Mechanical regulation of cell-cycle progression and division. *Trends Cell Biol.* **32**, P773–P785 (2022), https://doi.org/10.1016/j.tcb.2022.03.010.
13. N. Peela *et al.*, Advanced biomaterials and microengineering technologies to recapitulate the stepwise process of cancer metastasis. *Biomaterials* **133**, 176–207 (2017).
14. K. Wolf *et al.*, Collagen-based cell migration models in vitro and in vivo. *Semin. Cell Dev. Biol.* **20**, 931–941 (2009).
15. K. Wolf *et al.*, Physical limits of cell migration: Control by ECM space and nuclear deformation and tuning by proteolysis and traction force. *J. Cell Biol.* **201**, 1069–1084 (2013).
16. P. T. Caswell, T. Zech, Actin-based cell protrusion in a 3D matrix. *Trends Cell Biol.* **28**, 823–834 (2018).
17. M. Guo *et al.*, Cell volume change through water efflux impacts cell stiffness and stem cell fate. *Proc. Natl. Acad. Sci. U.S.A.* **114**, E8618–E8627 (2017).
18. S. Watkins, H. Sontheimer, Hydrodynamic cellular volume changes enable glioma cell invasion. *J. Neurosci.* **31**, 17250–17259 (2011).
19. X. Hao *et al.*, Acral lentiginous melanoma of foot and ankle: A clinicopathological study of 7 cases. *Anticancer Res.* **39**, 6175–6181 (2019).
20. P. P. Provenzano, S. R. Hingorani, Hyaluronan, fluid pressure, and stromal resistance in pancreas cancer. *Br. J. Cancer* **108**, 1–8 (2013).
21. T. Stylianopoulos *et al.*, Coevolution of solid stress and interstitial fluid pressure in tumors during progression: Implications for vascular collapse. *Cancer Res.* **73**, 3833–3841 (2013).
22. H.-P. Lee, R. Stowers, O. Chaudhuri, Volume expansion and TRPV4 activation regulate stem cell fate in three-dimensional microenvironments. *Nat. Commun.* **10**, 529 (2019).
23. Y. Li *et al.*, Compression-induced dedifferentiation of adipocytes promotes tumor progression. *Sci. Adv.* **6**, eaax5611 (2020).
24. X. Zhao, J. Hu, Y. Li, M. Guo, Volumetric compression develops noise-driven single-cell heterogeneity. *Proc. Natl. Acad. Sci. U.S.A.* **118**, e2110550118 (2021).
25. C. Roffay *et al.*, Passive coupling of membrane tension and cell volume during active response of cells to osmosis. *Proc. Natl. Acad. Sci. U.S.A.* **118**, e2103228118 (2021).
26. Y. Li *et al.*, Volumetric compression induces intracellular crowding to control intestinal organoid growth via Wnt/β-catenin signaling. *Cell Stem Cell* **28**, 170–172 (2021).
27. K. Bera *et al.*, Extracellular fluid viscosity enhances cell migration and cancer dissemination. *Nature* **611**, 365–373 (2022).
28. L. Hoen *et al.*, Osmotic stress interferes with DNA damage response and H2AX phosphorylation in human keratinocytes. *Cells* **11**, 959 (2022).
29. K. Meeth, J. X. Wang, G. Micevic, W. Damsky, M. W. Bosenberg, The YUMM lines: A series of congenic mouse melanoma cell lines with defined genetic alterations. *Pigment Cell Melanoma Res.* **29**, 590–597 (2016).
30. X. Zhang, T. Chan, M. Mak, Morphodynamic signatures of MDA-MB-231 single cells and cell doublets undergoing invasion in confined microenvironments. *Sci. Rep.* **11**, 6529 (2021).
31. X. Zhang, M. Mak, Biophysical informatics approach for quantifying phenotypic heterogeneity in cancer cell migration in confined microenvironments. *Bioinformatics* **37**, 2042–2052 (2021), https://doi.org/10.1093/bioinformatics/btab053.
32. J. Wang *et al.*, UV-induced somatic mutations elicit a functional T cell response in the YUMMER1.7 mouse melanoma model. *Pigment Cell Melanoma Res.* **30**, 428–435 (2017).
33. K. M. Stroka *et al.*, Water permeation drives tumor cell migration in confined microenvironments. *Cell* **157**, 611–623 (2014).
34. H. Li *et al.*, YAP/TAZ activation drives uveal melanoma initiation and progression. *Cell Rep.* **29**, 3200–3211.e4 (2019).
35. R. Gargini *et al.*, WIP drives tumor progression through YAP/TAZ-dependent autonomous cell growth. *Cell Rep.* **17**, 1962–1977 (2016).
36. Y. Zhang, X. Wang, Targeting the Wnt/β-catenin signaling pathway in cancer. *J. Hematol. Oncol.* **13**, 165 (2020).
37. L. D. Zorova *et al.*, Mitochondrial membrane potential. *Anal. Biochem.* **552**, 50–59 (2018).
38. R. Halaban *et al.*, PLX4032, a selective BRAF(V600E) kinase inhibitor, activates the ERK pathway and enhances cell migration and proliferation of BRAF melanoma cells. *Pigment Cell Melanoma Res.* **23**, 190–200 (2010).
39. M. Kalli, P. Papageorgis, V. Gkretsi, T. Stylianopoulos, Solid stress facilitates fibroblasts activation to promote pancreatic cancer cell migration. *Ann. Biomed. Eng.* **46**, 657–669 (2018).
40. O. R. Ajuwon, J. L. Marnewick, L. M. Davids, "Rooibos (*Aspalathus linearis*) and its major flavonoids–Potential against oxidative stress-induced conditions" in Basic Principles and Clinical Significance of Oxidative Stress (InTechOpen, 2015). https://doi.org/10.5772/61614.
41. H.-E. Kim, S.-G. Lee, Induction of ATP synthase β by H2O2 induces melanogenesis by activating PAH and cAMP/CREB/MITF signaling in melanoma cells. *Int. J. Biochem. Cell Biol.* **45**, 1217–1222 (2013).
42. M. Kleih *et al.*, Direct impact of cisplatin on mitochondria induces ROS production that dictates cell fate of ovarian cancer cells. *Cell Death Dis.* **10**, 851 (2019).
43. S.-Y. Kim *et al.*, Doxorubicin-induced reactive oxygen species generation and intracellular Ca^{2+} increase are reciprocally modulated in rat cardiomyocytes. *Exp. Mol. Med.* **38**, 535–545 (2006).
44. M. Zafarullah, W. Q. Li, J. Sylvester, M. Ahmad, Molecular mechanisms of N-acetylcysteine actions. *Cell. Mol. Life Sci.* **60**, 6–20 (2003).
45. P. Shah *et al.*, Nuclear deformation causes DNA damage by increasing replication stress. *Curr. Biol.* **31**, 753–765.e6 (2021).
46. C. Sun *et al.*, Genetic polymorphism of Slc31a1 is associated with clinical outcomes of platinum-based chemotherapy in non-small-cell lung cancer patients through modulating microRNA-mediated regulation. *Oncotarget* **9**, 23860–23877 (2018).
47. V. Vasiliou, K. Vasiliou, D. W. Nebert, Human ATP-binding cassette (ABC) transporter family. *Human Genomics* **3**, 281 (2008).
48. L. Kelland, The resurgence of platinum-based cancer chemotherapy. *Nat. Rev. Cancer* **7**, 573–584 (2007).
49. M. E. Dolega *et al.*, Cell-like pressure sensors reveal increase of mechanical stress towards the core of multicellular spheroids under compression. *Nat. Commun.* **8**, 14056 (2017).
50. H. T. Nia *et al.*, Solid stress and elastic energy as measures of tumour mechanopathology. *Nat. Biomed. Eng.* **1**, 0004 (2016).
51. H. K. Matthews, C. Bertoli, R. A. M. de Bruin, Cell cycle control in cancer. *Nat. Rev. Mol. Cell Biol.* **23**, 74–88 (2022).
52. P. J. van Diest, E. van der Wall, J. P. A. Baak, Prognostic value of proliferation in invasive breast cancer: A review. *J. Clin. Pathol.* **57**, 675–681 (2004).
53. N. M. Novikov, S. Y. Zolotaryova, A. M. Gautreau, E. V. Denisov, Mutational drivers of cancer cell migration and invasion. *Br. J. Cancer* **124**, 102–114 (2021).
54. N. Maddodi, A. Jayanthy, V. Setaluri, Shining light on skin pigmentation: The darker and the brighter side of effects of UV radiation. *Photochem. Photobiol.* **88**, 1075–1082 (2012).
55. T. L. de Jager, A. E. Cockrell, S. S. Du Plessis, Ultraviolet light induced generation of reactive oxygen species. *Adv. Exp. Med. Biol.* **996**, 15–23 (2017).
56. P. Meredith, J. Riesz, Radiative relaxation quantum yields for synthetic eumelanin. *Photochem. Photobiol.* **79**, 211–216 (2004).
57. S. S. Cao, R. J. Kaufman, Endoplasmic reticulum stress and oxidative stress in cell fate decision and human disease. *Antioxid. Redox Signal.* **21**, 396–413 (2014).
58. A. V. Snezhkina *et al.*, ROS generation and antioxidant defense systems in normal and malignant cells. *Oxid. Med. Cell. Longev.* **2019**, 6175804 (2019).
59. S. Ishida, J. Lee, D. J. Thiele, I. Herskowitz, Uptake of the anticancer drug cisplatin mediated by the copper transporter Ctr1 in yeast and mammals. *Proc. Natl. Acad. Sci. U.S.A.* **99**, 14298–14302 (2002).
60. A. K. Holzer, G. H. Manorek, S. B. Howell, Contribution of the major copper influx transporter CTR1 to the cellular accumulation of cisplatin, carboplatin, and oxaliplatin. *Mol. Pharmacol.* **70**, 1390–1394 (2006).
61. M. P. Ween, M. A. Armstrong, M. K. Oehler, C. Ricciardelli, The role of ABC transporters in ovarian cancer progression and chemoresistance. *Crit. Rev. Oncol. Hematol.* **96**, 220–256 (2015).
62. A. Subramanian *et al.*, Gene set enrichment analysis: A knowledge-based approach for interpreting genome-wide expression profiles. *Proc. Natl. Acad. Sci. U.S.A.* **102**, 15545–15550 (2005).
63. X. Zhang, Compression on Mus musculus Transcriptome. *National Center for Biotechnology Information* Sequence Read Archive, https://www.ncbi.nlm.nih.gov/bioproject/PRJNA982577, 06/12/2023.